Translational profiling of neuronal subtypes in pre-symptomatic fatal familial insomnia mice reveals TOR signaling in somatostatin-expressing neurons

Susanne Bauer
Linköping University: Linkopings universitet
Lars Dittrich
German Center for Neurodegenerative Diseases Site Göttingen: Deutsches Zentrum fur Neurodegenerative Erkrankungen Standort Gottingen
Lech Kaczmarczyk
Linköping University: Linkopings universitet
Melvin Schleif
German Center for Neurodegenerative Diseases Site Göttingen: Deutsches Zentrum fur Neurodegenerative Erkrankungen Standort Gottingen
Rui Benfeitas
Science for Life Laboratory: SciLifeLab
Walker S. Jackson (walker.jackson@liu.se)
Linköping University https://orcid.org/0000-0002-3003-5509

Research article

Keywords: Prion, fatal familial insomnia, Creutzfeldt-Jakob disease, RiboTag, somatostatin, selective vulnerability, neurodegeneration, transcriptome analysis, GSEA, co-expression network

Posted Date: March 25th, 2022

DOI: https://doi.org/10.21203/rs.3.rs-1458940/v1

Version of Record: A version of this preprint was published at Life Science Alliance on October 3rd, 2022. See the published version at https://doi.org/10.26508/lsa.202201530.

Abstract

Background

Selective neuronal vulnerability is a common, yet poorly understood characteristic of neurodegenerative diseases. It is particularly fascinating in familial prion diseases, such as fatal familial insomnia (FFI) and Creutzfeldt-Jakob disease (CJD), where different mutants of the prion protein manifest as clinically and neuropathologically distinct diseases.

Methods

To determine how distinct neurons respond to different mutations in the prion protein gene at pre-symptomatic stages, we used RiboTag to isolate cell type-specific, translating mRNA from GABAergic, glutamatergic, somatostatin- (SST) and parvalbumin- (PV) expressing neurons of 9-month-old knock-in mouse models of FFI and CJD. Differential gene expression analysis followed by gene set enrichment analysis (GSEA) was performed for all cell types in both diseases. We further constructed a undirected weighted gene co-expression network for SST neurons to identify functional models and hub genes.

Results

We found SST^+ neurons showed the most prominent gene expression changes in both diseases, especially in FFI, with high similarities between the two diseases. GSEA demonstrated similar enrichment patterns of functional terms for GABAergic cell types in both FFI and CJD, whereas responses in glutamatergic neurons were disease specific. For SST^+ neurons, functional analysis revealed upregulation of ribosomal biogenesis, mitochondrial function and neurodegenerative disease pathways, and downregulation of synaptic function and small GTPase mediated signaling in FFI. Analysis of an SST co-expression network revealed a disease-associated module, functionally associated with autophagy and TORC1 signaling. Of the identified module hub genes, three were further significantly differentially expressed in FFI SST neurons, including *Depdc5*, a component of mTOR regulator complex GATOR1, and Nucleosome Remodeling Deacetylase complex component *Mta3.* Importantly, the molecular changes reported here were very different from those reported for an acquired prion disease model.

Conclusions

This study identifies SST neurons as an early affected cell type, showing similar responses in both FFI and CJD with downregulation of mTOR signaling as a potential explanatory mechanism underlying many of the observed changes. The observation that FFI and CJD have such similar cellular and molecular signatures indicates that a common therapy may be effective for multiple inherited prion diseases, but possibly less effective for acquired prion disease.

Introduction

Neurodegenerative diseases (NDs) are widely thought to be caused by the misfolding of specific proteins. They tend to emerge in middle to late life and slowly, progressively destroy the brain, invariably causing

death. A striking feature of NDs is the selective vulnerability of specific neurons and brain regions in early disease stages, which occurs despite widespread expression of the disease-causing protein.

Selective vulnerability is particularly curious in the case of genetic prion diseases, where different point mutations in the ubiquitous prion protein (PrP) have been linked to different diseases affecting different brain regions and manifesting with distinct neuropathological hallmarks and clinical signs (1). Familial Creutzfeldt-Jakob disease (hereafter CJD, although it differs from non-familial forms) can be caused by several mutations but is most commonly linked to the E200K substitution (2). Clinical signs include rapidly progressing dementia, balance and gait disturbances, myoclonus, and sometimes seizures. Neuropathological hallmarks of CJD include spongiform degeneration accompanied by astrogliosis and neuronal loss in the cortex, deposition of PrP aggregates that resist proteinase K digestion (PrP^{res}), and mild spongiform degeneration in the molecular layer of the cerebellum (3),(4). The most common genetic prion disease is fatal familial insomnia (FFI), caused by a D178N substitution (5). This devastating disease typically begins with rapidly progressing insomnia, autonomic and motor disturbances, followed by cognitive decline (6),(4). Neuronal loss is most severe in the anterior and medial dorsal thalamus and accompanied by astrogliosis. However, in contrast to most other prion diseases, spongiform degeneration and PrP^{res} are typically absent and usually occur only in cases with a prolonged disease course (7). Cerebellar neuropathology includes gross atrophy (5), prominent loss of Purkinje cells and morphological changes to granular neurons (4). Remarkably, despite the expression of the mutant proteins throughout life, these inherited diseases usually emerge in middle to late life, the same age as other causes of PrDs even though the mutant protein is expressed throughout life.

Clinical signs of FFI and CJD correlate with loss of function of affected brain regions but the underlying mechanisms for these disease-specific patterns are unknown. In addition to regional vulnerability, certain cell types are highly vulnerable. Thus, rather than analyzing brain regions, an alternative approach is to analyze cell type-specific responses in the presence of mutated PrP. This can be accomplished by analyzing the translatome, mRNAs associated with ribosomes, from specific cell types. In this study, we analyzed translatome changes in four major neuronal subtypes, targeting broader groups of $vGluT2^{+}$ glutamatergic excitatory neurons and $Gad2^{+}$ GABAergic inhibitory neurons, as well as GABAergic subpopulations expressing neuropeptides PV or SST, which are typically non-overlapping. These are of particular interest for our study, since PV-expressing neurons in the cortex or cerebellum are highly vulnerable in PrDs (8)(9). Moreover, PV^{+} (10) and SST^{+} neurons (11)(12) are highly vulnerable in other NDs and psychiatric disorders (13). To obtain cell type-specific translatome profiles, we used RiboTag (14) directed to specific neuronal populations in knock-in mouse models of FFI and CJD at a pre-symptomatic stage. This experimental design resulted in several unexpected findings. Despite the vastly different regional pathologies, cell type specific responses were similar between FFI and CJD but were strikingly different from those in a model of acquired prion disease in which PrP was expressed from the same genetic locus. Also, we describe for the first time extensive transcriptional changes in SST^{+} neurons at pre-symptomatic disease stages, a cell type that has hitherto been understudied in PrDs.

Methods

Mouse lines

129S4 mice homozygous for the mouse equivalent of the D178N (FFI) (15) or E200K (CJD) (16) substitution and the 3F4 epitope (L108M, V11M) in the *Prnp* locus were studied. Due to deletion of a single codon at the N-terminus in the mouse *Prnp* gene, the mouse-equivalent nomenclature for these substitutions is D177N and E199K. PrD mice were crossed with RiboTag mice (B6N.129-Rpl22$^{tm1.1Psam}$/J, line #011029; Jackson Laboratory, Bar Harbor, ME) (14) and Cre-driver lines: Vglut2-IRES-Cre (17) (Slc17a6$^{tm2(cre)Lowl}$/J, line #016963; Jackson Laboratory), Gad2-IRES-Cre (18) (Gad2$^{tm2(cre)Zjh}$/J, line #010802; Jackson Laboratory), SST-IRES-Cre (18) (Sst$^{tm2.1(cre)Zjh}$/J, line #013044; Jackson Laboratory) and PV-IRES-Cre (19) (B6;129P2-Pvalb$^{tm1(cre)Arbr}$/J, line #008069; Jackson Laboratory). Prior to these crosses all lines were backcrossed to the 129S4 background, details in (20). This background was chosen since, unlike C57Bl/6 mice which can be hyperactive at night, 129S4 mice are relatively calm (20). We were concerned that mice with a non-uniform activity level would be prone to highly variable expression patterns. For cell type-specific targeting, mice double homozygous for *Prnp* and Cre were bred to mice double homozygous for *Prnp* and RiboTag, resulting in experimental mice all being homozygous for *Prnp* and double heterozygous for Cre and RiboTag. Mice were sacrificed at 9 months of age (mean age 9.3 months, SD: 0.7) by carbon dioxide asphyxiation between 10:00 a.m. and 14:00 p.m., matching time points for PrD and control mice to minimize the influence of circadian rhythm-related gene expression changes. Brains were separated into hemispheres along the midline. From one hemisphere the olfactory bulb was removed and discarded, the cerebellum was separated from the cerebrum, flash frozen in cryo-tubes on a dry-ice chilled metal block, and stored at -78°C. The second hemisphere was fixed in formalin.

Electroencephalography (EEG) and sleep recordings

The EEG/Sleep studies reported here were contemporaneous with another recent study of acquired prion disease (21), and experimental details can be found in that report. EEG and electromyograph detection leads were implanted in the epidural layer of the frontal cortex or in the neck muscles, respectively, and were routed subcutaneously to connect to telemetric recorders (F20-EET, Data Sciences International) that were implanted in the intraperitoneal cavity. Sleep scoring and analysis was done as reported before (22)(23)(24). Six-hour sleep deprivations were accomplished with the gentle handling method. The study group included 14 wild-type (mean age 20.6, SD 3.2 months), 15 FFI (mean age 20.8, SD 1.6 months), and 8 CJD (mean age 21.4, SD 1.2 months) mice. Several FFI mice died after the completion of the surgeries. It is possible these were more affected than the others and that the group successfully studied with EEG represent less affected mice.

Buffers and preparation of tissue homogenates

Stocks for polysome buffer (PSB; 50 mM Tris pH = 7.5, 100 mM KCl, 12 mM MgCl2, 1% IPEGAL CA-630 (Sigma-Aldrich, St. Louis MO), plus: 1 mM DTT, 60 U/ml RiboLock RNase inhibitor (ThermoScientific, Waltham MA), 100 µg/ml Cyclohexamide (Sigma-Aldrich, St. Louis MO), 2x SigmaFast EDTA-free protease inhibitor cocktail (Sigma-Aldrich, St. Louis MO) dissolved in PSB stock), high salt wash buffer (HSB; 50 mM Tris pH = 7.5, 300 mM KCl, 12 mM MgCl2, 1% IPEGAL, plus: 1 mM DTT, 20 U/ml RiboLock, 100 µg/ml Cyclohexamide and 0.5x EDTA-free SigmaFast protease inhibitor cocktail), and extra high salt buffer (EHSB; HSB containing additional 300 mM NaCl) were prepared using RNase-free reagents and stored at 4°C.

Inhibitors were added to stock solutions directly before use (indicated by “plus”). RNA purifications were performed in a Biosafety level 3 environment. Frozen tissue samples were homogenized at 450 rpm, using Wheaton Potter-Elvehjem homogenizers and PTFE pestles (DWK Life Science, Millville, NJ) with a motorized homogenizer (HEI-Torque Core, heidolph, Schwabach, Germany), in 200 µl ice-cold Polysome buffer per 0.01 g tissue. Homogenates were centrifuged at 4°C, 400xg for 2 min to collect nuclei. Supernatant was transferred to fresh vials and centrifuged at 4°C, 10000xg for 10 min.

Preparation of total RNA

Following preparation of homogenates as described above, the supernatant (S1) was decanted and 200 µl (cerebrum) or 100 µl S1 (cerebellum) were used to purify total RNA by adding 300 µl Trizol (Qiagen, Hilden, Germany) and 300 µl chloroform, vigorous shaking, and incubation for 5 min at room temperature (RT). Samples were centrifuged at 14000xg, RT, for 10 min, the aqueous phase was collected, mixed with 2x volume of 99,5% ethanol, 0.1x volume of 3 M sodium acetate (pH = 5.2) and GlycoBlue (ThermoScientific, Waltham MA; to 50 µg/ml final concentration), shaken vigorously and incubated at -20°C for 2 h. Nucleic acids were pelleted by centrifugation at 18000xg, 4°C for 15 min. Supernatant was discarded and pellets incubated for 30 min in 350 µl PKB buffer (4 M guanidinium isothiocyanate pH = 7.5, 0.1 M beta-mercaptoethanol, 25 mM sodium citrate and 0.5% Sarkosyl; pH < 7), to inactivate any potentially remaining prion infectivity. Resuspended pellets were transferred to a genomic DNA removal kit column (Qiagen, Hilden, Germany) and centrifuged for 20 s at 8000xg, RT. Flow trough was mixed with an equal volume of 70% ethanol, transferred to a RNeasy Mini kit column (Qiagen, Hilden, Germany) and prepared according to Qiagen protocol. Total RNA was eluted with 30 µl nuclease-free water and stored at -72°C.

RiboTag Immunoprecipitation

Prior to RiboTag purification, protein G-coated dynabeads (PGDB; Invitrogen, Waltham MA, Cat. 1009D, Lot: 00729875) were washed twice by resuspension in 1x PBS and once in PSB. IgG2b Isotype antibody (Invitrogen, Waltham MA; Cat. 14473285, Lot: 2025721), diluted 1:50 in PSB, was bound to washed beads by incubation on a MACSmix Tube Rotator (Miltenyi Biotec, Bergischgladbach, Germany) at 4°C, 20 min. Isotype Ab-bound beads were resuspended in 900 µl S1, incubated rotating for 30 min, 4°C, and collected on a Millipore Magna GrIP magnetic rack (Millipore, Burlington MA). The supernatant was incubated with 36 µl of anti-HA 12CA5 monoclonal antibody (Roche, Cat. 11666606001, Lot: 39746400), rotating at 4°C for 90 min. 90 µl washed PGDB were resuspended in the S1-antibody mix and incubated rotating at 4°C for 45 min. Beads were washed twice with 900 µl PSB, thrice with 900 µl HSB and once with 900 µl EHSB. For each wash step, beads were carefully resuspended in buffer and incubated at 300 rpm for 2–5 min (Thermomixer shaker; Eppendorf, Hamburg, Germany). To inactivate any remaining prion infectivity, washed beads were resuspended in 50 µl of PKB for 30 min, RT. 500 µl Qiazol (Qiagen, Hilden, Germany) were added and incubated at 300 rpm, RT, 10 min. Beads were collected on a magnetic rack and the supernatant moved to a fresh tube with 400 µl chloroform, shaken vigorously and incubated for 1 min, RT. Samples were centrifuged at 14000xg, RT, for 10 min, the aqueous phase moved to a fresh tube and mix with equal volume of 80% ethanol. RNA was extracted using Qiagen RNeasy micro columns (Qiagen, Hilden, Germany) according to protocol, eluted with 30 µl of nuclease-free water and stored at -72°C. To increase the RNA yield from SST^+ and PV^+ neurons, immunoprecipitation was performed in duplicates, using 900 µl S1 per IP. Following elution

from the PGDB, both duplicates were stepwise added to the same RNeasy micro kit column for RNA extraction.

Library preparation and sequencing

Libraries were prepared at SNP&SEQ Technology platform at NGI Uppsala, Sweden, using the Illumina TruSeq Stranded mRNA protocol. Quality control and quantification of RNA samples and libraries was performed using Agilent Tapestation (Agilent, Santa Clara CA). Paired end sequencing (100 bp) was performed on an Illumina NovaSeq6000 sequencer using a S4 flow cell (Illumina, San Diego CA). Libraries of two included samples (BK119.A and U84.A) failed initial sequencing and were resequenced at 150 bp PE and the same platform.

Data Availability

Code is openly available at github repository https://susannebauer.github.io/familialPrD/. Raw data is deposited on GEO with accession number GSE198063. (Author comment: Both the raw data and github repository will be made public upon publication. Pre-publication access for reviewers will be provided if requested.)

Nf-core pipeline

Alignment was performed using the nf-core/rnaseq 3.0 analysis pipeline (25) using default settings. STAR and Salmon were used for alignment and quantification. Sequences for ERCC spike ins and RiboTag-HA tag were included as additional Fasta file and are available on our github repository. Samples were kept if they contained > 30M mapped reads and < 20% ribosomal RNA reads. One *Prnp* wild-type SST^{+} sample (Z58.A) was excluded as we detected cross-contamination with *Prnp* reads containing the D178N mutation.

Marker enrichment and principal component analysis (PCA)

To generate PCA plots we calculated the variance for protein-coding genes based on log-scaled transcripts per million (TPM) values across either RiboTag IP or total RNA samples. Top 1% most variable genes were used for principal component analysis with prcomp() and visualized with ggplot2 (v3.3.3). Enrichment of cell type specific marker genes in IP and total RNA samples was analyzed using gene-wise z-score of log2-transformed TPM values and visualized using pheatmap (v1.0.12).

Differential gene expression analysis

Differential expression analysis was performed for each cell type comparing disease and control samples (FFI vs. WT and CJD vs. WT) with DESeq2 (v1.30.1)(26). Salmon transcript counts were collapsed to gene levels using tximport (v1.18.0) and prefiltered to include only protein coding genes with a row-wise mean count > 10. Genes with false discovery rate (FDR)-adjusted p-values ≤ 0.05 were considered differentially expressed, no log2 fold change (LFC) cutoff was applied. Results from DESeq2 included several genes with extreme LFCs which occurred due to highly variable expression with zero TPM values occurring in biological replicates in control and disease groups. These genes are likely non-informative and are not visualizated in dotplots in Fig. 4A + B by adjusting the y axis using the ggplot function coord_carthesian(). The original plots are shown in Additional File 5.

Overrepresentation analysis

Overrepresentation of genes from gene ontology (GO) classes included in Biological Process (BP), Cellular Compartment (CC), Molecular Function (MF) collection (2021), and KEGG Mouse pathways (2019) among differentially expressed genes (DEGs) was performed using the enrichR R package (v3.0). Terms with adjusted p-value ≤ 0.01 were considered significant.

Gene set enrichment analysis

Gene set enrichment analysis (GSEA) was performed for each cell type and disease using piano (v2.6.0) (27) for GO Biological Process (c5.go.bp.v7.4.symbols; gsea-msigdb.org) and KEGG pathways (KEGG_mouse_2019; maayanlab.cloud/Enrichr). KEGG pathways relating to tissues of different embryonic origin were removed from the list of genes sets, a detailed list of exclusion terms can be obtained from the "ReadMe.txt" file. Enrichment analysis was performed using runGSA() function setting DEseq2-derived p-values as 'geneLevelStats', LFC as 'directions', 'signifMethod = "geneSampling" ', 'adjMethod = "BH"' and limiting gene set size to 15–500 genes. Gene set statistics for different directionality classes were calculated using six methods by setting argument for "geneSetStats" to "mean", "median", "sum", "stouffer", "reporter" or "tailStrength". Median consensus scores were calculated based on adjusted p-values using the integrated consensusScores() function. Terms with distinct directional adjusted p values ≤ 0.05 in at least half of the applied gene set statistics were included in result tables. For Fig. 5, GO terms were collapsed to parent terms using rrvigo (v1.2.0) by semantic similarity ("Resnik", threshold = 0.8).

Topological network analysis

A co-expression weighted network was constructed by calculating the pairwise spearman rho correlation between protein-coding genes with mean TPM > 10 across samples, excluding genes with the lowest 20% variance across samples. Positive correlations (FDR ≤ 0.01) were used to construct a weighted gene co-expression network with igraph (v1.2.6) of 6960 nodes and 616054 edges, using spearman rho as edge weights. Community analysis was performed using the Leiden algorithm (28)(leiden v0.3.7), setting partition type to modularity vertex partition and setting the weights argument to edge weights. Clustering results were compared to a random network of equal size generated using the Erdos-Renyi G(n,M) model. Enrichment analysis for genes of the six main modules was performed using enrichR (v3.0) (29). For plotting of top-ranked gene sets (Fig. S5), enriched terms (FDR ≤ 0.01) were ranked by combined score (30). igraph was used to calculate centralities. Network plots were generated using Cytoscape (v3.8.2). Hub genes were defined as top 1% nodes with highest degree centrality for each module.

Protein-protein interaction (PPI) network

To validate interactions of identified hub genes, we constructed a protein-protein interaction (PPI) network for hub genes and first neighbors using STRING interaction and functional enrichment data (using STRINGdb plug-in for Cytoscape), including PPIs with a combined confidence score ≥ 0.7, excluding interaction data based on text mining and database.

Results

We previously developed knock-in mouse models of familial CJD and FFI linked to E200K and D178N mutations, in the endogenous mouse *Prnp* gene (15)(16). These models developed late onset, progressive diseases that replicate several key pathological features of the respective human diseases, and importantly, differ from each other in pathological changes and affected brain regions. FFI mice experience neuronal loss and reactive astrocytosis in the thalamus and atrophied cerebellum (15). In contrast, CJD mice develop PrP^{res} and spongiosis, hallmarks of the human disease, most prominently in the hippocampus, and PrP^{res} in the molecular layer of the cerebellum (31) (Fig. 1A). PrP in CJD mice had a slightly altered glycoform pattern, suggesting a slightly altered path through the secretory system, but in FFI mice, mono- and unglycosylated PrP were nearly absent and the total amount of all forms was only 25% of normal levels (15), suggesting it is subjected to intensive quality controls and that the mammalian brain responds to these mutant proteins differently. Automated mouse behavioral analysis indicated sleep was fragmented and core body temperature measurements suggested FFI mice had impaired sleep regulation at this age (32), but electroencephalography (EEG) measurements were not attempted then due to biosafety constraints. Consideration of the neuropathological changes and *in vivo* clinical abnormalities measured by automated behavioral analysis and *in vivo* magnetic resonance imaging led to the general picture that disease emerged at approximately 16 months of age for both models (31)(15).

Neural activity is mildly affected in old FFI and CJD mice

To rigorously characterize the general neural health and sleep features in these models, we used the same EEG methods (Fig. 1B) we applied previously to the RML (Rocky Mountain Labs) model of acquired PrD (21). Since this was a telemetric recording system, mice could roam freely in their cage, thereby avoiding artifacts from tethering. In that study, theta frequency waves increased as disease progressed, like observations in several human PrDs (33). Notably, sleep was not affected in RML mice, even in late stages (21). Turning to the FFI mice, since we previously observed that behavioral activity was only mildly affected at 16 months of age, which is likely a result of only mildly diminished neural health at that timepoint, to increase the likelihood of detecting EEG abnormalities we studied mice at approximately 21 months of age (mean = 20.8, SD = 2.3). Surprisingly, considering that in FFI mice temperature was dysregulated and that sleep bouts were disrupted according to an automated video-based system (15), sleep was not strongly affected in the current EEG study. During daytime, non-rapid eye movement (NREM) sleep tended to be reduced, and wake tended to be increased, but neither was significant (Fig. 2). To test if sleep control was vulnerable to external manipulation, we measured the response to six hours of sleep deprivation, which showed no significant differences between FFI and control mice (Additional File 1A + B). Since sleep abnormalities are sometimes absent in humans with FFI (5)(34), their absence from this mouse model is not a complete surprise. CJD mice were studied in parallel, and they also showed no abnormality in baseline sleep (Fig. 2C + D) or in response to sleep deprivation (Additional File 1C + D). Nonetheless, theta frequency waves were increased in FFI mice during NREM and REM sleep (Fig. 2F + G), and in CJD mice during wake and REM sleep (Fig. 2H + J), mimicking this potential biomarker of human PrD. Therefore, despite these models showing neuropathological and behavioral changes at this stage, there are only mild changes to theta frequency and the disease is still too mild to cause sleep disruption.

In our recent RML study mentioned above (21), we found that before EEG, behavioral or neuropathological changes emerged, RiboTag profiling identified specific cell types with altered translatomes. To study a similar disease stage as done for that study (56% of disease onset), these RiboTag experiments included mice at nine months of age.

Capture of cell type-specific mRNA with RiboTag

With RiboTag, cell type-specific translatomes are obtained from homogenates of brain tissue by immunoprecipitating HA-tagged ribosomes and the attached translating mRNA. Driver lines expressing Cre directed by the genes encoding Gad2 (35), vGluT2 (17), PV (19) and SST (35) were used to achieve cell type-specific expression of the RiboTag transgene (Fig. 1C). This enabled us to target wider populations of glutamatergic and GABAergic neurons, as well as PV^+ and SST^+ GABAergic subtypes. Using a selection of cell type marker genes, we recently confirmed by both immunofluorescence and RNA-seq of RiboTag IPs, that these Cre lines lead to specific and selective activation of RiboTag expression (21). Since the cerebellum was affected in both FFI and CJD models, and the remaining part of the brain (hereafter cerebrum) had distinct brain regions that were targeted in each model, the cerebellum and cerebrum from each brain were frozen separately. RiboTag IPs were prepared for all cell types for cerebrum samples, but only for Gad2 and vGluT2 for cerebellum, since in the cerebellum PV-Cre induces RiboTag expression in the same cells as Gad2-Cre, whereas SST-Cre induces RiboTag expression in very few cells. Consequently, we profiled six cell types, encompassing two brain regions, in two genetic PrDs (Fig. 1D, Additional File 2). To verify the isolation of cell type specific translatomes in RiboTag samples, we additionally analyzed total mRNA from the homogenates in parallel (Fig. 1D). The study group was age-matched (mean = 9.3 months, SD = 0.7), double heterozygous for RiboTag and Cre, and homozygous for either FFI, CJD, or WT *Prnp* alleles (Additional File 3).

As expected, PCA showed differences between total mRNA samples based on the region (cerebellar vs cerebral) but not cell types (Fig. 3A). In contrast, IP samples showed clear differences based on regions and cell types (Fig. 3B). This was apparent through comparisons of expression of cell type marker genes between IP and total mRNA, which revealed the expected enrichment of general GABAergic and glutamatergic neuronal marker genes in samples in which the respective cell types were targeted (Fig. 3C + D). Targeting of specific subclasses of GABAergic neurons was confirmed by upregulation of PV- or SST-specific marker genes in the respective samples, whereas *Htr3a* (serotonin receptor 3A) and *Vip* (vasoactive intestinal peptide), GABAergic markers absent from SST and PV neurons, showed the predicted enrichment in $Gad2^+$ and depletion in PV^+ and SST^+ IPs (Fig. 3C). In the cerebellum, $Gad2^+$ IPs were enriched for marker genes of several cerebellar GABAergic cell types such as Purkinje, basket, Golgi, and stellate cells, while $vGluT2^+$ IPs showed enrichment for granule cell markers (Fig. 3D) (36)(37). As expected, astrocyte and microglia marker genes (38) were depleted in all IP samples. These results indicate that cell type-specific translating mRNA was successfully isolated from the intended neuronal subpopulations.

Prnp expression varies with cell type and sequence

One potential explanation for selective vulnerability is that vulnerable cell types express high levels of toxic protein. To test this possibility, we examined the expression levels of *Prnp* in the targeted cell types based on TPM values (Fig. 3E). Unexpectedly, *Prnp* was expressed almost two-fold higher in $vGluT2^+$ neurons than in

GABAergic cell types. These differences were detected in all three genotypes. Higher *Prnp* expression in vGluT2 neurons may partially explain the selective vulnerability in these models since the regions most affected, thalamus and hippocampus, are predominately glutamatergic. This analysis also showed that FFI mice had slightly lower *Prnp* expression. This tendency was most pronounced in glutamatergic neurons and only significant in cerebral vGluT2$^+$ neurons (Kruskal-Wallis, $p = 0.026$, $chi^2 = 7.312$). This observation is consistent with the reduced PrP levels previously reported in FFI mouse brains, suggesting that the D178N mutant engages either a different or more intensive quality control mechanism than the E200K mutant. Since the protein levels are reduced much more than the mRNA levels, the protein misfolding may be happening during and after mRNA translation and both get triaged for degradation.

SST$^+$ neurons show pronounced translatome changes in pre-symptomatic stages of CJD and FFI

A general characterization of translatome profiles for disease-targeted cell types in both disease models was done by differential gene expression analysis with the DESeq2 R package (26) (Additional File 4). Since the mice were at a pre-symptomatic disease stage, we expected mild changes to gene expression and therefore defined differentially expressed genes (DEGs) to have a false discovery rate (FDR) ≤ 0.05 without a log fold change (LFC) cutoff (Fig. 4A + B, Additional File 5A + B). Surprisingly, SST$^+$ neurons responded with the highest number of DEGs in both disease models (CJD: 153, FFI: 684), whereas PV$^+$ neurons showed very few DEGs (CJD: 2, FFI: 3). A comparison of shared DEGs between cell types of the same disease revealed that most DEGs were unique to a given cell type, including GABAergic subtypes (Fig. 4C + D). In contrast, SST$^+$ neurons demonstrated a high overlap in DEGs between CJD and FFI, with 55 down- and 58 upregulated genes shared (Fig. 4E). There were few shared genes in other cell types, likely due to the overall low number of DEGs (Additional File 5C). Since little is known about the vulnerability of SST$^+$ neurons to PrDs, many of our analyses focused on these important cells.

In both mutants, SST$^+$ neurons displayed increased expression of many ribosomal protein mRNAs: of 79 ribosomal proteins, 26 were upregulated in CJD (mean log2FC = 0.42, SD = 0.09) and 57 in FFI (mean LFC = 0.44, SD = 0.09) (Additional File 5D). Besides suggesting an increased need to synthesize proteins, the high functional connectivity of these genes is strongly indicative of a coordinated response. To measure the coordination amongst other DEGs we looked for enriched GO classes by applying ORA. Upregulated DEGs In CJD SST$^+$ neurons were associated with translation (ribosomal protein genes), actin cytoskeleton, actin-filament organization, and axonogenesis (FDR ≤ 0.01, Additional Files 6 + 7). In FFI SST$^+$ neurons upregulated DEGs were mostly related to translation (*Snu13, Eef1a1, Eef12* and several ribosomal proteins (Additional Files 7 + 8A)). Upregulated DEGs were overrepresented in “myelination”, and cytoskeleton and cell adhesion-related terms, including “actin-binding”, “focal adhesion” and “cell-substrate junction”. Notably, downregulated DEGs in FFI SST$^+$ neurons were also enriched among cytoskeleton-associated terms (“processes related to neurite morphogenesis and organization” term, “microtubule binding” and “motor activity”) and cell adhesion. Additionally, downregulated genes were overrepresented among terms related to synaptic plasticity and ion-channels or receptor components (Additional file 8B). We also found enrichment of GTPase activity, including genes involved in Ras and Rho signaling, such as activators of Rho-family

GTPases (*Arhgap32,35,44)*, Rho guanine nucleotide exchange factors (GEFs) (*Als2, Agap2, Trio, Dock4*), and downstream effectors *(Cdc42bpa, Rock2).* Rho GTPases are known regulators of actin cytoskeleton dynamics (reviewed here: (39)), including dendritic spine formation and density (40), further indicating a high connectivity between DEGs. Collectively, these results suggest a concerted effort to reorganize the cytoskeleton of SST^+ neurons. In summary, CJD and FFI showed a surprisingly high overlap in DEGs and, to a lesser extent, in enriched GO terms, suggesting that these neurons activate similar responses in both diseases.

Gene set enrichment analysis reveals similar functional enrichments in CJD and FFI

A limitation of ORA is that coordinated but statistically insignificant expression changes of several genes within a pathway may have important biological implications but would be excluded. Therefore, we applied a complementary approach, gene set enrichment analysis (GSEA) (41), to assess enrichment of GO terms for biological processes (BP) and KEGG pathways in each cell type, using the piano R package (27) which provides combined enrichment scores summarizing results of several statistical methods. Additionally, separate p-values for different directionalities of change were provided for each gene set. Gene sets with significant up- or down-regulation (FDR $\leq$ 0.05) were ranked by their consensus score, which was calculated based on adjusted p-values for all six statistical methods applied (Additional File 9). Only gene sets significant in at least three of the six statistical methods are presented in Fig. 5.

Top ranked gene sets for CJD and FFI SST^+ neurons showed upregulation of translation-related gene sets and ND-related pathways, including “Alzheimer’s disease”, “Parkinson’s disease”, and “oxidative phosphorylation”. Shared downregulated terms included “axon extension”, “neuron differentiation”, “positive regulation of neuron projection development” and “synapse organization”. FFI SST^+ neurons also showed downregulation of pathways and terms related to synaptic function, phosphatidylinositol phosphorylation, and downregulation of “small GTPase mediated signaling transduction” (Fig. 5 column 3). Therefore, the results of these analyses reflect DESeq and ORA results for SST^+ neurons despite methodological differences.

Interestingly, GSEA results also showed similar enrichment patterns for PV^+ neurons in both disease models (Fig. 5, column 2), which were missed by DESeq and ORA due to the low number of DEGs (Fig. 4A + B). As with SST^+ neurons, we found upregulation of translation-related pathways and GO terms, but not changes of ND-related pathways. Both disease models showed upregulation of immune response-related pathways, and downregulation of phosphatidylinositol-signaling, “positive regulation of autophagy”, and “protein processing in the endoplasmic reticulum” (ER). Downregulated GO terms exclusive to FFI PV^+ neurons suggested a disruption in synaptic function (“synapse organization”, “Axon guidance”, “positive regulation of neuron projection development”). Interestingly, “neuron migration”, “neuron differentiation”, and “regulation of cell shape” were upregulated in CJD but downregulated in FFI PV^+ neurons (Fig. 5, column 2). Compared to the highly similar enrichment patterns observed in PV^+ and SST^+ neurons, $Gad2^+$ neurons of the cerebrum were less similar between the disease models. In FFI we observed upregulation of ribosome pathway, GTPase signaling (Ras and Rap1), neuron migration and inflammation-related GO terms, whereas in CJD

terms related to metabolic processes, mitochondrial translation, proteasome, and DNA repair were downregulated (Fig. 5, column 1). In contrast, Gad2$^+$ neurons of the cerebellum exhibited widespread changes with similar patterns in each model (Fig. 5, column 5). Both disease models showed upregulation of terms related to translation, splicing, RNA and protein transport, and ND related pathways. GO terms and pathways related to phosphatidylinositol and GTPase signaling, inflammation and cellular morphology ("regulation of cell shape", "Cell adhesion molecules"), neuron migration and differentiation were downregulated in both diseases.

In contrast to the broadly similar changes in GABAergic neurons, vGluT2$^+$ neurons of the cerebrum showed more disease-specific responses (Fig. 5, column 4). For example, in CJD, ND pathways, oxidative phosphorylation, chromatin organization and axon extension are enriched among downregulated genes. In contrast, FFI showed downregulation of ER protein processing and protein export neuron differentiation, and neuropeptide signaling. Notably, positive regulation of GTPase activity, phosphatidylinositol phosphorylation and chromatin organization had different directionalities between the diseases. Shared responses included downregulation of mRNA transport and upregulation of small GTPase activity and aminoacyl-tRNA biosynthesis. Cerebellar vGluT2$^+$ neurons displayed the most pronounced differences between models, with several gene sets exhibiting opposite regulation between CJD and FFI, such as those related to translation, DNA repair, and mRNA transport, which were down in CJD but up in FFI. We further found downregulation of ND pathways, splicing, protein folding, and starvation response unique to CJD. In contrast, FFI vGluT2$^+$ neurons showed upregulation of apoptosis and regulation of mitotic cell cycle, and downregulation of ER protein processing and synaptic function (Fig. 5, column 6). Overall, GSEA revealed high similarities in enriched ontologies and pathways between the diseases for SST$^+$, PV$^+$ and cerebellar Gad2$^+$ neurons, but in vGluT2$^+$ neurons, especially in the cerebellum, it demonstrated disease-specific responses.

Identification of functional modules in an SST$^+$ co-expression network

Since SST neurons are understudied in PrD research, we wondered if they might reveal new insights into therapeutic targets. Thus, we used a network-based approach to further elucidate patterns in gene expression changes in SST$^+$ neurons. Using our SST$^+$ neuron-specific translatome data we constructed an undirected weighted gene co-expression network using pairwise gene correlations (FDR $\leq$ 0.01, Spearman $\rho > 0.82$) (Additional File 10). Community analysis using Leiden algorithm (28) generated six major modules (ranging in size from 249 to 2,733 genes) consisting of genes with highly correlated expression patterns across all conditions (Fig. 6A), which were validated by comparison to a random network. As co-expression analysis builds on the assumption that correlation patterns between genes reflect functional connection, we used ORA to determine significantly enriched (FDR $\leq$ 0.01) ontology terms and pathways among module genes (Additional File 11).

Module 1 consisted predominantly of genes downregulated in both diseases (Fig. 6A), including 241 genes also differentially expressed, and predominantly downregulated, in FFI. Module genes were significantly overrepresented (FDR $\leq$ 0.01) among terms related to synaptic transmission, protein modifications and transport, response to starvation, neuron projection development and axon guidance. Module genes

annotated to these terms also included several genes which we identified as differentially expressed either in both diseases (indicated in bold italics in Fig. 6A) or specific for FFI (italics). Genes annotated to synapse organization, chromatin remodeling, and regulation of dephosphorylation-related terms included FFI-specific DEGs. Interestingly, ORA of module 1 genes also revealed autophagy-regulation ("negative regulation of macroautophagy" and "TORC1 signaling") and chromatin modifications ("positive regulation of histone ubiquitination") among the top enriched ontologies (Additional File 12A).

Module 2 genes were enriched for translation, ribosomal biogenesis, and mitochondrial organization (Additional File 12B, Fig. 6A). This is consistent with ORA results from upregulated DEGs identified in CJD and FFI SST^+ neurons (Additional Files 6 + 8), as module 2 contains ribosomal protein genes, a large percentage of which were upregulated in both diseases. Additional enriched GO terms related to ER stress, regulation of apoptotic process-related terms, and unfolded protein response (UPR), which included several FFI-specific DEGs such as *activating transcription factors 4* and *5, Atf4* and *Atf5* (Fig. 6A). These results are consistent with those from GSEA (Fig. 5) and functional analysis of cell type specific DEGs (Additional Files 6 + 8). This indicates genes in modules 1 and 2 might be of particular interest to familial PrD-associated pathological processes as these show highly correlated expression patterns with a high percentage of DEGs and are functionally closely related to identified dysregulated terms.

Genes in Module 3 were mostly downregulated in both diseases and functionally associated with chemical synaptic transmission, nervous system development, and protein modifications (Fig. 6A) but also including translation initiation, regulation of macroautophagy and stress granule assembly among top enriched GO terms (Additional File 12C). Module 4 was highly connected with Module 3 and contained predominantly upregulated genes associated with ER organization, protein targeting and ubiquitination (Fig. 6A, Additional File 12D). Module 4 also contained several mitochondrial genes, in particular encoding ATP synthase subunits, associated with KEGG pathways oxidative phosphorylation, thermogenesis and Alzheimer's and Parkinson's disease pathways (Fig. 6A). Module 5 genes showed significant overrepresentation of terms related to mRNA splicing and RNA processing (Fig. 6A, Additional File 12E). No significant enrichment was detected for genes in module 6.

Hub genes point towards two potential therapeutic targets

To find potentially important regulators, we next identified hub genes that display the largest number of co-expressed genes. We defined hubs as the top 1% of genes with the highest degree centrality, i.e., most direct neighbors, in each module of our co-expression network (Table 1). Notably, three hub genes in Module 1 were also differentially expressed in FFI: GATOR1 subunit *Depdc5* (*DEP Domain containing Complex 5;* degree: 560), histone-deacetylase *Mta3* (Metastasis Associated 1 Family Member 3; degree: 551) a subunit of the nucleosome remodeling and deacetylase (NuRD) complex, and *Gtf3c1* (General Transcription Factor IIIC Subunit 1; degree: 585) a mediator of RNA polymerase III transcription. Since downregulation of these highly connected hub genes suggests they have a central role in the pathological process that may have far-reaching effects on interaction partners, we next aimed to further validate the interaction of hub genes with their co-regulated neighbors. For this we constructed a protein-protein interaction (PPI) network for each hub gene and its first-degree neighbors, to determine whether known interactions between products of co-

regulated genes exist. Predicted PPIs were obtained from STRINGdb, considering only interactions with a high combined confidence score ≥ 0.7, and excluding interactions based on text mining and databases.

There were no predicted interactions of *Gtf3c1* with its co-regulated direct neighbors, indicating that this method did not provide further insight for this gene. However, the PPI network for *Mta3* included 220 of 551 co-regulated genes from our topological network (Additional File 13) while the PPI network for *Depdc5* included 230 of 560 co-regulated genes (Fig. 6B, Additional File 14). Both networks additionally showed strong overlap with 145 shared genes and included 30 genes significantly downregulated in FFI (Fig. 6B, blue border) or 2 in both diseases (green border). Pathway and GO enrichment analysis using the STRING Enrichment application (FDR ≤ 0.05) revealed association of *Depdc5* PPI-network genes with autophagy, chromatin organization, vesicle-mediated transport, and neurite morphology (axonogenesis, synapse organization), ribonucleoprotein complex biogenesis, and tRNA metabolic process. *Depdc5* and its direct neighbors in the PPI network were associated with TORC1 signaling. Given the far-reaching effects of mTOR signaling on metabolic regulation and autophagy, its involvement in ageing and proposed involvement in neurodegeneration, we propose this may be a central regulator behind translatome changes we observed in SST^+ neurons in familial PrD. Taken together, this analysis indicates that for both diseases SST^+ neurons show the largest response with TORC1 signaling posing a potential underlying regulatory mechanism.

Discussion

Here we report the translatome responses of six neuronal cell types in knock-in mouse models of two genetic PrDs at a pre-symptomatic stage. We expected to see different responses of cells to different diseases and were therefore surprised by the high similarities. In both disease models, SST^+ neurons had the highest number of DEGs, 74% of which were shared between CJD and FFI. Furthermore, additional levels of similarity between CJD and FFI emerged from ORA and GSEA studies, e.g., upregulation of translation, ND pathways, and actin-binding proteins, suggesting the disease mechanisms are similar in both models. Since SST^+ neurons showed more DEGs in FFI than in CJD, and a functional analysis revealed downregulation of genes related to synaptic function and GTPase signaling, SST^+ neurons in FFI brains appear to be at a more advanced disease stage.

Previous reports indicated a pronounced early loss of cortical PV^+ neurons in patients and models of sporadic, familial and variant CJD, although they are relatively spared in FFI patients (42), perhaps reflecting that the cortex is usually less affected in FFI. Based on their reported early vulnerability and the hypothesis that transcriptional changes precede neuronal pathology and loss (21), we expected to observe more pronounced gene expression changes in PV^+ neurons, at least for CJD mice, but this was not apparent based on the number of DEGs. However, GSEA of FFI PV^+ neurons revealed enrichment in gene sets that could be associated with neuronal dysfunction, such as ER protein processing or synapse organization, suggesting PV^+ neurons are mildly affected early in this model. Importantly, we observed similar changes in SST^+ neurons, a cell type that has previously not been implicated in PrD pathology.

In contrast, GSEA results for cerebellar neurons displayed widespread changes of major pathways and functional processes, despite few DEGs detected for both neuron types in FFI and $vGluT2^+$ neurons in CJD.

This suggests there is a moderate but coordinated response, in line with early neuropathological changes in the cerebellum observed in both diseases. Our analyses show high similarities in enriched terms, and their directionalities, between disease models in cerebellar Gad2$^+$ neurons, suggesting shared mechanisms underlying the pathology in these cells. In contrast, cerebellar vGluT2$^+$ neurons showed disease-specific responses. Further studies to confirm these results and determine their role for cerebellar pathology would be well placed. Overall, our findings indicate that SST$^+$ neurons are a previously unrecognized neuronal subtype affected early in FFI and CJD. Since vulnerability of SST$^+$ subpopulations has been described in other NDs (11), but not in PrDs, a deeper exploration of how these neurons responded in FFI and CJD was performed.

mTORC1 inhibitors are downregulated in SST$^+$ neurons

To further elucidate potential mechanisms and regulatory factors underlying the observed translatome changes in SST$^+$ neurons, we sought to identify topological modules and central genes by constructing a weighted gene-correlation network. These results indicated downregulation of TORC1 inhibitors, which likely lead to SST$^+$ neuron-specific activation of mTOR signaling, a positive regulator of protein synthesis, synaptogenesis, and negative regulator of autophagy. Thus, this single pathway may be responsible for many of the DEGs in SST$^+$ neurons.

Genes central in regulating TORC1 activity were differentially expressed in FFI SST$^+$ neurons, and the main TORC1 inhibitor, *Tsc1*, was downregulated in both disease models. Moreover, SST$^+$ neurons in both models showed expression changes consistent with increased mTOR activity, including upregulated expression of ribosomal and mitochondrial genes, downregulation of autophagy, and cytoskeletal reorganization. Topological network analysis of SST$^+$ samples indicated *Depdc5* as one of the module 1 hub genes. *Depdc5*, which was also significantly downregulated in FFI, encodes a subunit of the TORC1 inhibitor complex GATOR1, involved in amino acid-dependent TORC1 activation, and is associated with epilepsy. Haploinsufficiency of *Depdc5* causes aberrant morphology and TORC1 hyperactivation in induced pluripotent stem cells (43), suggesting that downregulation of *Depdc5* in our model may have considerable impact, despite the mild fold change. Histone deacetylase 6, *Hdac6*, which was down-regulated in FFI and strongly co-expressed with *Depdc5*, is suggested to be a modulator of TORC1 signaling (44) and central in inducing autophagy as a compensatory mechanism for impaired ubiquitin-proteasome system degradation (45). Over-expression of *Hdac6* in cortical neurons exposed to a toxic PrP fragment (PrP$^{106–126}$) was shown to increase cell survival by inducing autophagy through mTOR signaling modulation (44). Together, these points support the notion that mTOR signaling is affected in PrDs, and that it may be specific for SST neurons early in disease.

Aberrant activity of mTOR signaling has been demonstrated in many NDs, including Alzheimer's disease, Parkinson's disease, Huntington's disease and PrDs (46)(47). The central role of mTOR activity together with the availability of approved mTOR inhibitors such as rapamycin and derivatives has made it an attractive drug target and has been proposed as a disease modulating treatment approach for neurodegeneration and cognitive decline. While studies report positive effects of mTOR inhibitor treatment on cognition by enhancing autophagy and promoting clearance of protein aggregates, its overall role in neurodegeneration is

more complex. mTOR activity is an example of antagonistic pleiotropy, showing beneficial effects early in life at the expense of negative effects later in life, by promoting synaptogenesis during youth at the expense of increased risk of damage by protein accumulation due to autophagy inhibition (reviewed in (48)). This complicates using mTOR inhibition as a therapeutic strategy as its beneficial effects will likely depend on correct timing in the disease progression (49). Our data further highlight that cell type-specific differences in mTOR activity play an important role on whether intervention of mTOR inhibition results in overall positive or negative effects and therapies may need to be targeted to specific cell types.

Conclusion

Our results demonstrate a pronounced response of SST^+ neurons to early, pre-symptomatic stages of FFI, with a marked, coordinated up-regulation of mitochondrial and ribosome biogenesis-associated genes and down-regulation of cytoskeletal proteins or regulator genes. We identified 67 candidate module hub genes in a co-expression network of SST^+ neurons, of which three (*Gtf3c1, Depdc5* and *Mta3*) also showed differential expression in FFI and were therefore further validated. With a clear connection to mTOR signaling, a tentative pharmacologically targetable pathway can now be proposed for FFI and CJD and can be tested experimentally in the future.

We also report FFI and CJD to be more similar at the molecular level than predicted from differences in clinical signs and neuropathological changes. This was particularly true for SST^+ neurons, which have thus far been largely ignored in PrD research. Interestingly, we recently reported that SST^+ neurons showed little, if any, response to a widely studied mouse model (RML) of acquired PrD. Moreover, the genes and pathways changed in Gad2 and vGluT2 cells in RML brains (21) were completely different from those in FFI and CJD brains, indicating that the genetic and acquired diseases are unexpectedly different. Glutamatergic neurons showed the largest differences between FFI and CJD. For the cerebrum this now makes sense and in part can explain the selective vulnerability reported previously since each disease causes neuropathological changes in different brain regions, thalamus and hippocampus, especially enriched in glutamatergic neurons. However, in the cerebellum nearly all glutamatergic neurons are granule cells, a very homogeneous cell type, but they demonstrated strikingly different responses between the diseases. A unifying explanation of the causes of selective vulnerability remains elusive but continued experimentation with methods like RiboTag or Tagger (50) may help to eventually solve this mystery.

Abbreviations

BP	Biological process
CC	Cellular compartment
CJD	Creutzfeldt-Jakob disease
DEG	Differentially expressed gene
EEG	Electroencephalography

EMG	Electromyography
ER	Endoplasmic reticulum
FDR	False discovery rate
FFI	Fatal familial insomnia
GABA	Gamma aminobutyric acid
GO	Gene ontology
GSEA	Gene set enrichment analysis
IP	Immunoprecipitation
KEGG	Kyoto Encyclopedia of Genes and Genomes
LFC	Log2 fold change
MF	Molecular function
mTOR	Mammalian/mechanistic target of rapamycin
ND	Neurodegenerative disease
NREM	Non-rapid eye movement
ORA	Overrepresentation analysis
PCA	Principal component analysis
PPI	Protein-protein interaction
PrD	Prion disease
PrP	Prion protein
PV	Parvalbumin
REM	Rapid eye movement
RML	Rocky Mountain Laboratory prion strain
SST	Somatostatin
UPR	Unfolded protein response
TORC1	Target of rapamycin complex 1

Declarations

The authors would like to thank the National Genomics Infrastructure (NGI) for providing assistance with library preparation and sequencing. Computations and data handling were enabled by resources provided by the Swedish National Infrastructure for Computing (SNIC) at UPPMAX, partially funded by the Swedish Research Council through grant agreement no. 2018-05973. Support provided through the Swedish Bioinformatics Advisory Program organized by National Bioinformatics Infrastructure Sweden (NBIS) is gratefully acknowledged.

Author's contributions

Conceptualization and study design was performed by W.S.J. Tissue samples were collected by L.K., M.S., L.D. and W.S.J. Measurements and analyses of EEG and EMG data were performed by L.D. RiboTag purifications were performed by S.B. Processing and analysis of transcriptomics data was performed by S.B. with guidance from R.B. The manuscript was written by S.B. and W.S.J. with comments from all authors.

Funding

This work was supported by the Knut and Alice Wallenberg foundation and the German Center for Neurodegenerative Diseases.

Availability of data and materials

All code is freely and openly available at github repository https://susannebauer.github.io/familialPrD/. Raw data is deposited on GEO with accession number GSE198063.

Ethics approval and consent to participate

Mouse experiments were performed following national and local guidelines and were approved by local authorities LANUV-NRW with protocols84-02.04.2013.A128 and 84-02.04.2013.A169.

Competing interests

The authors declare that they have no competing interests.

Consent for publication

All authors consented to the publication of this work.

References

1. Jackson WS. Selective vulnerability to neurodegenerative disease: the curious case of Prion Protein. Dis Model Mech [Internet]. 2014 Jan;7(1):21–9. Available from: https://pubmed.ncbi.nlm.nih.gov/24396151.

2. Ladogana A, Kovacs GG. Chapter 13 - Genetic Creutzfeldt–Jakob disease. In: Pocchiari M, Manson JBT-H of CN, editors. Human Prion Diseases [Internet]. Elsevier; 2018. p. 219–42. Available from: https://www.sciencedirect.com/science/article/pii/B9780444639455000131.
3. Gambetti P, Kong Q, Zou W, Parchi P, Chen SG. Sporadic and familial CJD: Classification and characterisation. Br Med Bull. 2003;66:213–39.
4. Schmitz M, Dittmar K, Llorens F, Gelpi E, Ferrer I, Schulz-Schaeffer WJ, et al. Hereditary Hum Prion Diseases: Update Mol Neurobiol. 2017;54(6):4138–49.
5. Medori R, Tritschler HJ, LeBlanc A, Villare F, Manetto V, Chen HY, et al. Fatal familial insomnia, a prion disease with a mutation at codon 178 of the prion protein gene. N Engl J Med [Internet]. 1992;326(7):444–9. Available from: http://www.ncbi.nlm.nih.gov/entrez/query.fcgi?cmd=Retrieve&db=PubMed&dopt=Citation&list_uids=1346338.
6. Cracco L, Appleby BS, Gambetti P. Chapter 15 - Fatal familial insomnia and sporadic fatal insomnia. In: Pocchiari M, Manson JBT-H of CN, editors. Human Prion Diseases [Internet]. Elsevier; 2018. p. 271–99. Available from: https://www.sciencedirect.com/science/article/pii/B9780444639455000155.
7. Parch P, Petersen RB, Chen SG, Autilio-Gambetti L, Capellari S, Monari L, et al. Molecular pathology of fatal familial insomnia. Brain Pathol. 1998;8(3):539–48.
8. Guentchev M, Groschup MH, Kordek R, Liberski PP, Budka H. Severe, early and selective loss of a subpopulation of GABAergic inhibitory neurons in experimental transmissible spongiform encephalopathies. Brain Pathol. 1998;8(4):615–23.
9. Guentchev M, Wanschitz J, Voigtlander T, Flicker H, Budka H. Selective neuronal vulnerability in human prion diseases. Fatal familial insomnia differs from other types of prion diseases. Am J Pathol [Internet]. 1999;155(5):1453–7. Available from: https://www.ncbi.nlm.nih.gov/pubmed/10550300.
10. Holley SM, Galvan L, Kamdjou T, Cepeda C, Levine MS. Striatal GABAergic interneuron dysfunction in the Q175 mouse model of Huntington's disease. Eur J Neurosci. 2019;49(1):79–93.
11. Schmid LC, Mittag M, Poll S, Steffen J, Wagner J, Geis HR, et al. Dysfunction of Somatostatin-Positive Interneurons Associated with Memory Deficits in an Alzheimer's Disease Model. Neuron. 2016;92(1):114–25.
12. Ramos B, Baglietto-Vargas D, Rio JC, del, Moreno-Gonzalez I, Santa-Maria C, Jimenez S, et al. Early neuropathology of somatostatin/NPY GABAergic cells in the hippocampus of a PS1 × APP transgenic model of Alzheimer's disease. Neurobiol Aging. 2006;27(11):1658–72.
13. Sibille E, Morris HM, Kota RS, Lewis DA. GABA-related transcripts in the dorsolateral prefrontal cortex in mood disorders. Int J Neuropsychopharmacol. 2011;14(6):721–34.
14. Sanz E, Yang L, Su T, Morris DR, McKnight GS, Amieux PS. Cell-type-specific isolation of ribosome-associated mRNA from complex tissues. Proc Natl Acad Sci U S A. 2009 Aug;106(33):13939–44.
15. Jackson WS, Borkowski AW, Faas H, Steele AD, King OD, Watson N, et al. Spontaneous generation of prion infectivity in fatal familial insomnia knockin mice. Neuron. 2009 Aug;63(4):438–50.
16. Jackson WS, Borkowski AW, Watson NE, King OD, Faas H, Jasanoff A, et al. Profoundly different prion diseases in knock-in mice carrying single PrP codon substitutions associated with human diseases. Proc

Natl Acad Sci U S A [Internet]. 2013/08/21. 2013;110(36):14759–64. Available from: http://www.ncbi.nlm.nih.gov/pubmed/23959875.

17. Vong L, Ye C, Yang Z, Choi B, Chua S, Lowell BB. Leptin Action on GABAergic Neurons Prevents Obesity and Reduces Inhibitory Tone to POMC Neurons. Neuron [Internet]. 2011;71(1):142–54. Available from: http://dx.doi.org/10.1016/j.neuron.2011.05.028.
18. Haimon Z, Volaski A, Orthgiess J, Boura-Halfon S, Varol D, Shemer A, et al. Re-evaluating microglia expression profiles using RiboTag and cell isolation strategies. Nat Immunol. 2018;19(6):636–44.
19. Hippenmeyer S, Vrieseling E, Sigrist M, Portmann T, Laengle C, Ladle DR, et al. A developmental switch in the response of DRG neurons to ETS transcription factor signaling. PLoS Biol. 2005;3(5):0878–90.
20. Kaczmarczyk L, Reichenbach N, Blank N, Jonson M, Dittrich L, Petzold GC, et al. Slc1a3-2A-CreERT2 mice reveal unique features of Bergmann glia and augment a growing collection of Cre drivers and effectors in the 129S4 genetic background. Sci Rep. 2021 Mar;11(1):5412.
21. Kaczmarczyk L, Schleif M, Dittrich L, Williams R, Koderman M, Bansal V, et al. Simultaneous pathway engagement of translation in astrocytes, circadian rhythm in GABAergic neurons and cytoskeleton in glutamatergic neurons precede electroencephalographic changes in neurodegenerative prion disease. bioRxiv [Internet]. 2021 Jan 1;2021.11.26.470101. Available from: http://biorxiv.org/content/early/2021/11/27/2021.11.26.470101.abstract.
22. Morairty SR, Dittrich L, Pasumarthi RK, Valladao D, Heiss JE, Gerashchenko D, et al. A role for cortical nNOS/NK1 neurons in coupling homeostatic sleep drive to EEG slow wave activity. Proc Natl Acad Sci U S A [Internet]. 2013;110(50):20272–7. Available from: https://www.ncbi.nlm.nih.gov/pubmed/24191004.
23. Dittrich L, Morairty SR, Warrier DR, Kilduff TS. Homeostatic sleep pressure is the primary factor for activation of cortical nNOS/NK1 neurons. Neuropsychopharmacology [Internet]. 2015;40(3):632–9. Available from: https://www.ncbi.nlm.nih.gov/pubmed/25139062.
24. Parks GS, Warrier DR, Dittrich L, Schwartz MD, Palmerston JB, Neylan TC, et al. The Dual Hypocretin Receptor Antagonist Almorexant is Permissive for Activation of Wake-Promoting Systems. Neuropsychopharmacology [Internet]. 2016;41(4):1144–55. Available from: https://www.ncbi.nlm.nih.gov/pubmed/26289145.
25. Ewels PA, Peltzer A, Fillinger S, Patel H, Alneberg J, Wilm A, et al. The nf-core framework for community-curated bioinformatics pipelines. Vol. 38, Nature biotechnology. United States; 2020. pp. 276–8.
26. Love MI, Huber W, Anders S. Moderated estimation of fold change and dispersion for RNA-seq data with DESeq2. Genome Biol [Internet]. 2014;15(12):550. Available from: https://doi.org/10.1186/s13059-014-0550-8.
27. Väremo L, Nielsen J, Nookaew I. Enriching the gene set analysis of genome-wide data by incorporating directionality of gene expression and combining statistical hypotheses and methods. Nucleic Acids Res [Internet]. 2013 Apr 1;41(8):4378–91. Available from: https://doi.org/10.1093/nar/gkt111.
28. Traag VA, Waltman L, van Eck NJ. From Louvain to Leiden: guaranteeing well-connected communities. Sci Rep. 2019;9(1):1–12.

29. Kuleshov MV, Jones MR, Rouillard AD, Fernandez NF, Duan Q, Wang Z, et al. Enrichr: a comprehensive gene set enrichment analysis web server 2016 update. Nucleic Acids Res [Internet]. 2016 Jul 8;44(W1):W90–7. Available from: https://doi.org/10.1093/nar/gkw377.
30. Chen EY, Tan CM, Kou Y, Duan Q, Wang Z, Meirelles GV, et al. Enrichr: interactive and collaborative HTML5 gene list enrichment analysis tool. BMC Bioinformatics [Internet]. 2013;14(1):128. Available from: https://doi.org/10.1186/1471-2105-14-128.
31. Jackson WS, Borkowski AW, Watson NE, King OD, Faas H, Jasanoff A, et al. Profoundly different prion diseases in knock-in mice carrying single PrP codon substitutions associated with human diseases. Proc Natl Acad Sci U S A. 2013 Sep;110(36):14759–64.
32. Steele AD, Jackson WS, King OD, Lindquist S. The power of automated high-resolution behavior analysis revealed by its application to mouse models of Huntington's and prion diseases. Proc Natl Acad Sci U S A [Internet]. 2007;104(6):1983–8. Available from: https://www.ncbi.nlm.nih.gov/pubmed/17261803.
33. Franko E, Wehner T, Joly O, Lowe J, Porter MC, Kenny J, et al. Quantitative EEG parameters correlate with the progression of human prion diseases. J Neurol Neurosurg Psychiatry [Internet]. 2016/07/15. 2016;87(10):1061–7. Available from: https://www.ncbi.nlm.nih.gov/pubmed/27413165.
34. Zarranz JJ, Digon A, Atares B, Rodriguez-Martinez AB, Arce A, Carrera N, et al. Phenotypic variability in familial prion diseases due to the D178N mutation. J Neurol Neurosurg Psychiatry [Internet]. 2005;76(11):1491–6. Available from: http://www.ncbi.nlm.nih.gov/entrez/query.fcgi?cmd=Retrieve&db=PubMed&dopt=Citation&list_uids=16227536.
35. Taniguchi H, He M, Wu P, Kim S, Paik R, Sugino K, et al. A Resource of Cre Driver Lines for Genetic Targeting of GABAergic Neurons in Cerebral Cortex. Neuron. 2011;71(6):995–1013.
36. Tam WY, Wang X, Cheng ASK, Cheung KK. In search of molecular markers for cerebellar neurons. Int J Mol Sci. 2021;22(4):1–11.
37. Kozareva V, Martin C, Osorno T, Rudolph S, Guo C, Vanderburg C, et al. A transcriptomic atlas of mouse cerebellar cortex comprehensively defines cell types. Nature [Internet]. 2021;598(7879):214–9. Available from: http://dx.doi.org/10.1038/s41586-021-03220-z.
38. Saudou F, Humbert S. The Biology of Huntingtin. Neuron. 2016;89(5):910–26.
39. Sastre AA, Montoro ML, Gálvez-Martín P, Lacerda HM, Lucia A, Llavero F, et al. Small gtpases of the ras and rho families switch on/off signaling pathways in neurodegenerative diseases. Int J Mol Sci. 2020;21(17):1–23.
40. Ueda S, Negishi M, Katoh H. Rac. GEF dock4 interacts with cortactin to regulate dendritic spine formation. Mol Biol Cell. 2013;24(10):1602–13.
41. Subramanian A, Tamayo P, Mootha VK, Mukherjee S, Ebert BL, Gillette MA, et al. Gene set enrichment analysis: A knowledge-based approach for interpreting genome-wide expression profiles. Proc Natl Acad Sci [Internet]. 2005 Oct 25;102(43):15545 LP – 15550. Available from: http://www.pnas.org/content/102/43/15545.abstract.
42. Guentchev M, Wanschitz J. Short Communication Selective Neuronal Vulnerability in Human. Am J Pathol. 1999;155(5):1453–7.

43. Klofas LK, Short BP, Snow JP, Sinnaeve J, Rushing GV, Westlake G, et al. DEPDC5 haploinsufficiency drives increased mTORC1 signaling and abnormal morphology in human iPSC-derived cortical neurons. Neurobiol Dis [Internet]. 2020;143(May):104975. Available from: https://doi.org/10.1016/j.nbd.2020.104975.
44. Du Y, Wang F, Zou J, Le W, Dong Q, Wang Z, et al. Histone deacetylase 6 regulates cytotoxic α-synuclein accumulation through induction of the heat shock response. Neurobiol Aging [Internet]. 2014;35(10):2316–28. Available from: http://dx.doi.org/10.1016/j.neurobiolaging.2014.04.029.
45. Pandey UB, Nie Z, Batlevi Y, McCray BA, Ritson GP, Nedelsky NB, et al. HDAC6 rescues neurodegeneration and provides an essential link between autophagy and the UPS. Nature. 2007;447(7146):859–63.
46. Xu Y, Tian C, Wang S, Bin, Xie WL, Guo Y, Zhang J, et al. Activation of the macroautophagic system in scrapie-infected experimental animals and human genetic prion diseases. Autophagy. 2012;8(11):1604–20.
47. Perluigi M, Di Domenico F, Butterfield DA. mTOR signaling in aging and neurodegeneration: At the crossroad between metabolism dysfunction and impairment of autophagy. Neurobiol Dis. 2015;84:39–49.
48. Norwitz NG, Querfurth H. mTOR Mysteries: Nuances and Questions About the Mechanistic Target of Rapamycin in Neurodegeneration. Front Neurosci. 2020;14(July):1–10.
49. Querfurth H, Lee HK. Mammalian/mechanistic target of rapamycin (mTOR) complexes in neurodegeneration. Mol Neurodegener. 2021;16(1):1–25.
50. Kaczmarczyk L, Bansal V, Rajput A, Rahman R-U, Krzyżak W, Degen J, et al. Tagger-A Swiss army knife for multiomics to dissect cell type-specific mechanisms of gene expression in mice. PLoS Biol. 2019 Aug;17(8):e3000374.

Tables

Table 1: Hub genes for SST neuron co-expression network.

Hub genes were defined as top 1% of genes with highest degree centrality in each module. The last columns indicate log2 fold changes of hub genes and adjusted p-value (FDR) in FFI samples compared to wild-type controls.

Gene	Module	DEG	Description	Entrez ID	LFC (FFI)	FDR (FFI)
Depdc5	1	FFI	DEP domain containing 5	277854	-0.4078	0.0096
Gtf3c1	1	FFI	general transcription factor III C 1	233863	-0.3991	0.0189
Mta3	1	FFI	metastasis associated 3	116871	-0.3837	0.0215
Abcf2	1	neither	ATP-binding cassette, sub-family F (GCN20), member 2	27407	-0.191	0.2543
Abcg4	1	neither	ATP binding cassette subfamily G member 4	192663	-0.1572	0.3968
Abr	1	neither	active BCR-related gene	109934	-0.1583	0.3333
Adar	1	neither	adenosine deaminase, RNA-specific	56417	-0.2753	0.0665
Cabin1	1	neither	calcineurin binding protein 1	104248	-0.2813	0.1105
Carm1	1	neither	coactivator-associated arginine methyltransferase 1	59035	-0.1128	0.5449
Dab2ip	1	neither	disabled 2 interacting protein	69601	-0.1931	0.2543
Dusp8	1	neither	dual specificity phosphatase 8	18218	-0.1254	0.514
Gba2	1	neither	glucosidase beta 2	230101	-0.2639	0.1263
Kcnq2	1	neither	potassium voltage-gated channel, subfamily Q, member 2	16536	-0.2268	0.1584
Kdm4a	1	neither	lysine (K)-specific demethylase 4A	230674	-0.3135	0.0563
Kif1a	1	neither	kinesin family member 1A	16560	-0.3211	0.0624
Map3k4	1	neither	mitogen-activated protein kinase kinase kinase 4	26407	-0.2906	0.0816
Nol6	1	neither	nucleolar protein family 6 (RNA-associated)	230082	-0.2643	0.1356
Osbp2	1	neither	oxysterol binding protein 2	74309	-0.2788	0.089
Pdxk	1	neither	pyridoxal (pyridoxine, vitamin B6) kinase	216134	-0.2316	0.1489
Pdzd4	1	neither	PDZ domain containing 4	245469	-0.2219	0.1808
Ptprs	1	neither	protein tyrosine phosphatase, receptor type, S	19280	-0.267	0.1095
Rap1gap	1	neither	Rap1 GTPase-activating protein	110351	-0.2164	0.2388
Rusc2	1	neither	RUN and SH3 domain	100213	-0.331	0.054

			containing 2			
Smarca2	1	neither	SWI/SNF related, matrix associated, actin dependent regulator of chromatin, subfamily a, member 2	67155	-0.1895	0.2628
Tecpr1	1	neither	tectonin beta-propeller repeat containing 1	70381	-0.2488	0.1649
Vps11	1	neither	VPS11, CORVET/HOPS core subunit	71732	-0.2809	0.0974
Wdr81	1	neither	WD repeat domain 81	192652	-0.24	0.1874
Bola2	2	neither	bolA-like 2 (E. coli)	66162	0.1598	0.3747
Cbarp	2	neither	calcium channel, voltage-dependent, beta subunit associated regulatory protein	100503659	0.1118	0.5978
Chgb	2	neither	chromogranin B	12653	-0.0514	0.8321
Clstn1	2	neither	calsyntenin 1	65945	-0.0957	0.6549
Clstn3	2	neither	calsyntenin 3	232370	0.0567	0.8178
Eno2	2	neither	enolase 2, gamma neuronal	13807	0.0224	0.9305
Erp29	2	neither	endoplasmic reticulum protein 29	67397	0.2004	0.2832
Mlf2	2	neither	myeloid leukemia factor 2	30853	0.1074	0.582
Mtch1	2	neither	mitochondrial carrier 1	56462	0.1217	0.5536
Ndufaf2	2	neither	NADH:ubiquinone oxidoreductase complex assembly factor 2	75597	0.1683	0.3876
Nomo1	2	neither	nodal modulator 1	211548	-0.0515	0.8354
Pomgnt2	2	neither	protein O-linked mannose beta 1,4-N-acetylglucosaminyltransferase 2	215494	-0.0482	0.8468
Psmd4	2	neither	proteasome (prosome, macropain) 26S subunit, non-ATPase, 4	19185	0.1939	0.2965
Rab3a	2	neither	RAB3A, member RAS oncogene family	19339	0.1032	0.6085
Tmsb10	2	neither	thymosin, beta 10	19240	0.1508	0.4312
Tomm7	2	neither	translocase of outer mitochondrial membrane 7	66169	0.1699	0.3821
Abca5	3	neither	ATP-binding cassette, sub-family A (ABC1), member 5	217265	-0.0966	0.6559

Appbp2	3	neither	amyloid beta precursor protein (cytoplasmic tail) binding protein 2	66884	-0.0543	0.8261
Cdc27	3	neither	cell division cycle 27	217232	-0.0475	0.8426
Dpp10	3	neither	dipeptidylpeptidase 10	269109	-0.0441	0.8597
Dzip3	3	neither	DAZ interacting protein 3, zinc finger	224170	-0.0347	0.8885
Mctp1	3	neither	multiple C2 domains, transmembrane 1	78771	-0.0424	0.8659
Nampt	3	neither	nicotinamide phosphoribosyltransferase	59027	-0.0451	0.854
Nr1d2	3	neither	nuclear receptor subfamily 1, group D, member 2	353187	-0.0234	0.9282
Rab1a	3	neither	RAB1A, member RAS oncogene family	19324	0.0018	0.9937
Zdhhc17	3	neither	zinc finger, DHHC domain containing 17	320150	-0.0592	0.8072
Azin1	4	neither	antizyme inhibitor 1	54375	-0.0302	0.9057
Negr1	4	neither	neuronal growth regulator 1	320840	-0.0148	0.9557
Pten	4	neither	phosphatase and tensin homolog	19211	-0.034	0.8881
Rab10	4	neither	RAB10, member RAS oncogene family	19325	-0.0315	0.9035
Rab14	4	neither	RAB14, member RAS oncogene family	68365	-0.0073	0.98
Septin7	4	neither	septin 7	235072	-0.0231	0.9258
Slc25a16	4	neither	solute carrier family 25 (mitochondrial carrier, Graves disease autoantigen), member 16	73132	0.0129	0.9613
Slc38a2	4	neither	solute carrier family 38, member 2	67760	-0.0063	0.9823
Slc6a15	4	neither	solute carrier family 6 (neurotransmitter transporter), member 15	103098	0.0247	0.9254
Ccdc82	5	neither	coiled-coil domain containing 82	66396	-0.2945	0.096
Ythdc1	5	neither	YTH domain containing 1	231386	0.0531	0.8308
Hpcal4	6	neither	hippocalcin-like 4	170638	0.0515	0.7933

Parva	6	neither	parvin, alpha		57342	-0.0184	0.9347

Figures

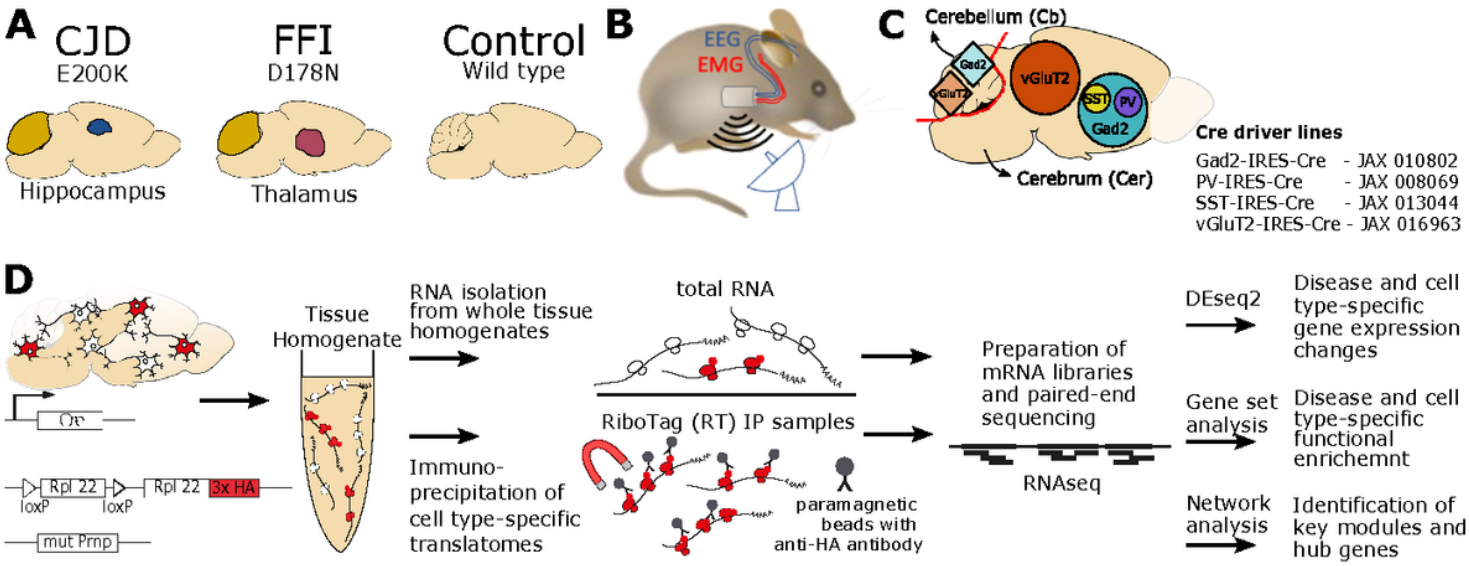

Figure 1

Experimental setup and workflow.

(A) We performed transcriptional profiling on two mutant Prnp knock-in mouse models of familial prion diseases, Creutzfeldt Jakob disease (CJD) and fatal familial insomnia (FFI) and compared to age-matched wildtype (WT) controls. Mutant Prnp mice show selective vulnerability in the hippocampus (blue) and thalamus (red), respectively. Both diseases also show secondary pathology in the Cerebellum (yellow). (**B**) Telemetric electroencephalography (EEG) and electromyography (EMG) were performed in CJD and FFI mice at 18-20 months of age to characterize the sleep phenotype. (**C**) Cre-driver lines were used to target neuronal subtypes in the Cerebellum (Cb), and Cerebrum without olfactory bulb (Cer). Gad2: Glutamate decarboxylase 2 marks GABAergic (gamma aminobutyric acid) neurons; vGluT2: vesicular Glutamate Transporter 2 marks glutamatergic neurons; PV (parvalbumin) and SST (somatostatin) target mutually exclusive subtypes of GABAergic neurons. (**D**) Schematic workflow for preparation and analysis of cell type-specific RiboTag IP samples and total RNA input control samples.

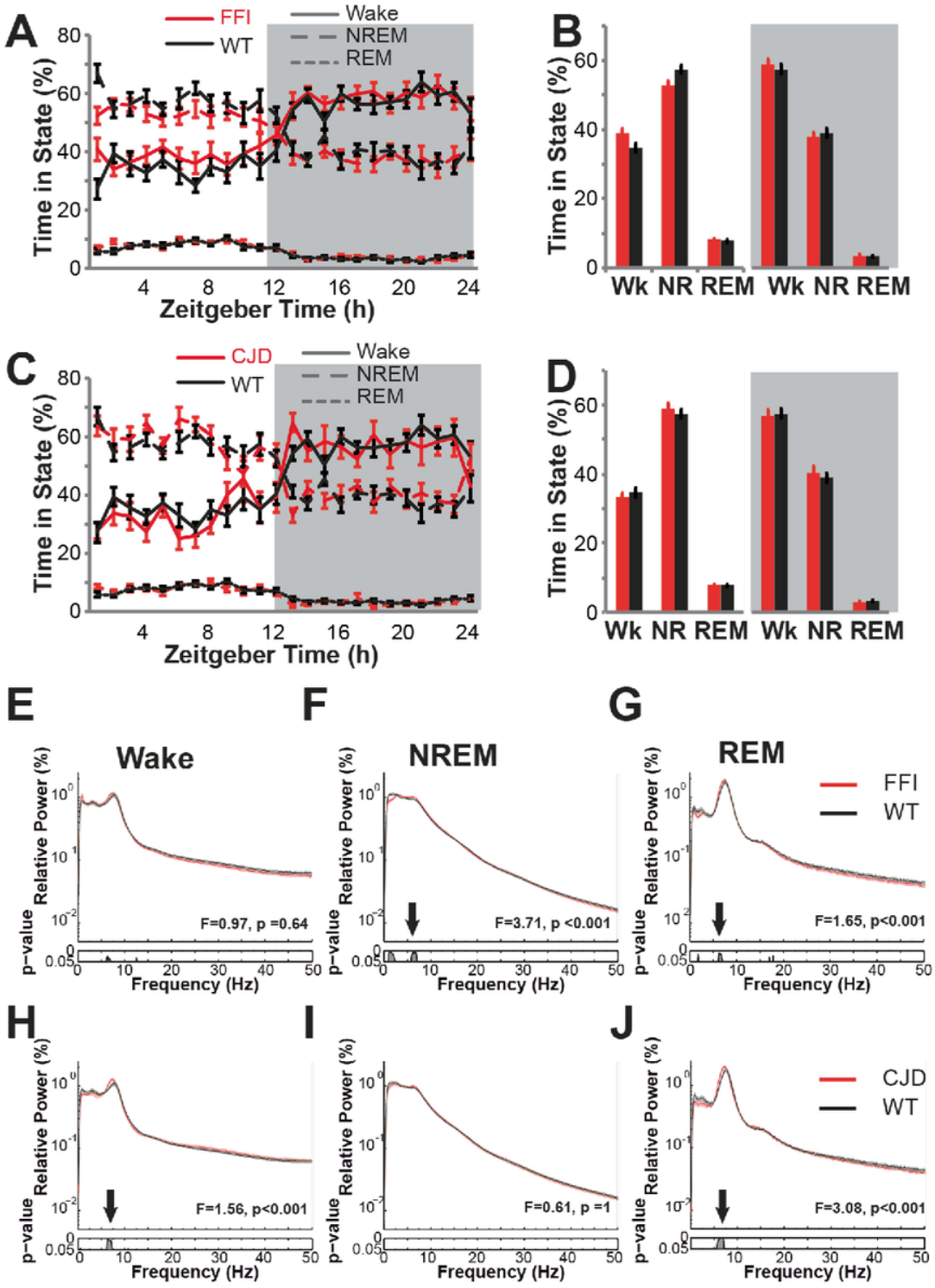

Figure 2

Aged FFI and CJD mice have mild EEG abnormalities.

(A) Baseline recordings covering 24 hours were divided into 10 sec windows and scored as Wake, NREM or REM, then pooled into 1-hour bins. The data were charted beginning when lights turn on (Zeitgeber Time 0); the gray background represents the dark cycle. The sleep states in FFI mice (Red lines) generally matched the sleep states in WT mice (black lines) across all bins. **(B)** Pooling data into 12-hour bins representing the

complete dark phase (grey background) or light phase (blank background) further shows FFI mice are very similar to WT in Wake (Wk), NREM (NR) and REM. (**C, D)** The same analytical procedure applied to CJD mice shows they are also similar to WT mice. (**E-J)** Power-frequency spectra depict, for each wave frequency (X-axis), the proportion of power (Y-axis) that it contributes to the full spectrum measured (0-50 Hz). Downward arrows indicate that theta band frequencies (5-10 Hz) are increased in FFI during NREM (F) and REM (G) sleep and increased in CJD mice in Wake (H) and REM (J) sleep.

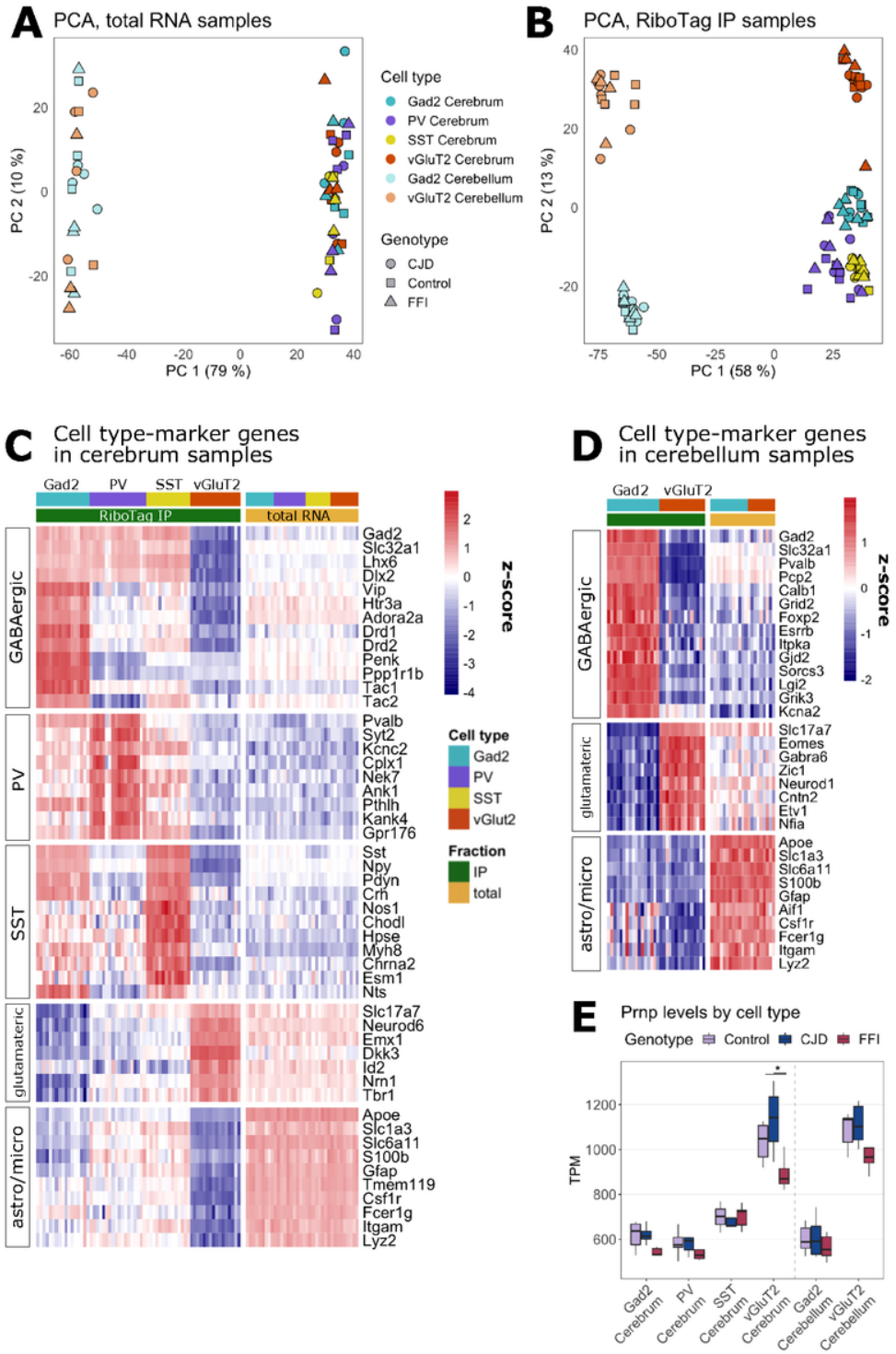

Figure 3

Cell type-specific translatome isolation with RiboTag Immunoprecipitation (IP).

Principal component analysis (PCA) of total RNA samples **(A)** and IP samples **(B)** show IP samples clustering by targeted cell type. PCA plots are based on top 1% most variable protein-coding genes. (**C, D**) Heatmap showing enrichment of cell type-specific marker genes in IP and total RNA samples obtained from Cerebrum (C) and Cerebellum (D). Row-wise Z scores were calculated across all samples based on TPM values. (**E**) *Prnp* expression levels were comparable between cell types for mutant *Prnp* and control mice in GABAergic neurons (Gad2). Glutamatergic (vGluT2) neurons showed significantly lower *Prnp* expression levels in FFI mice (Kruskal-Wallis, p = 0.026, chi2 = 7.312).

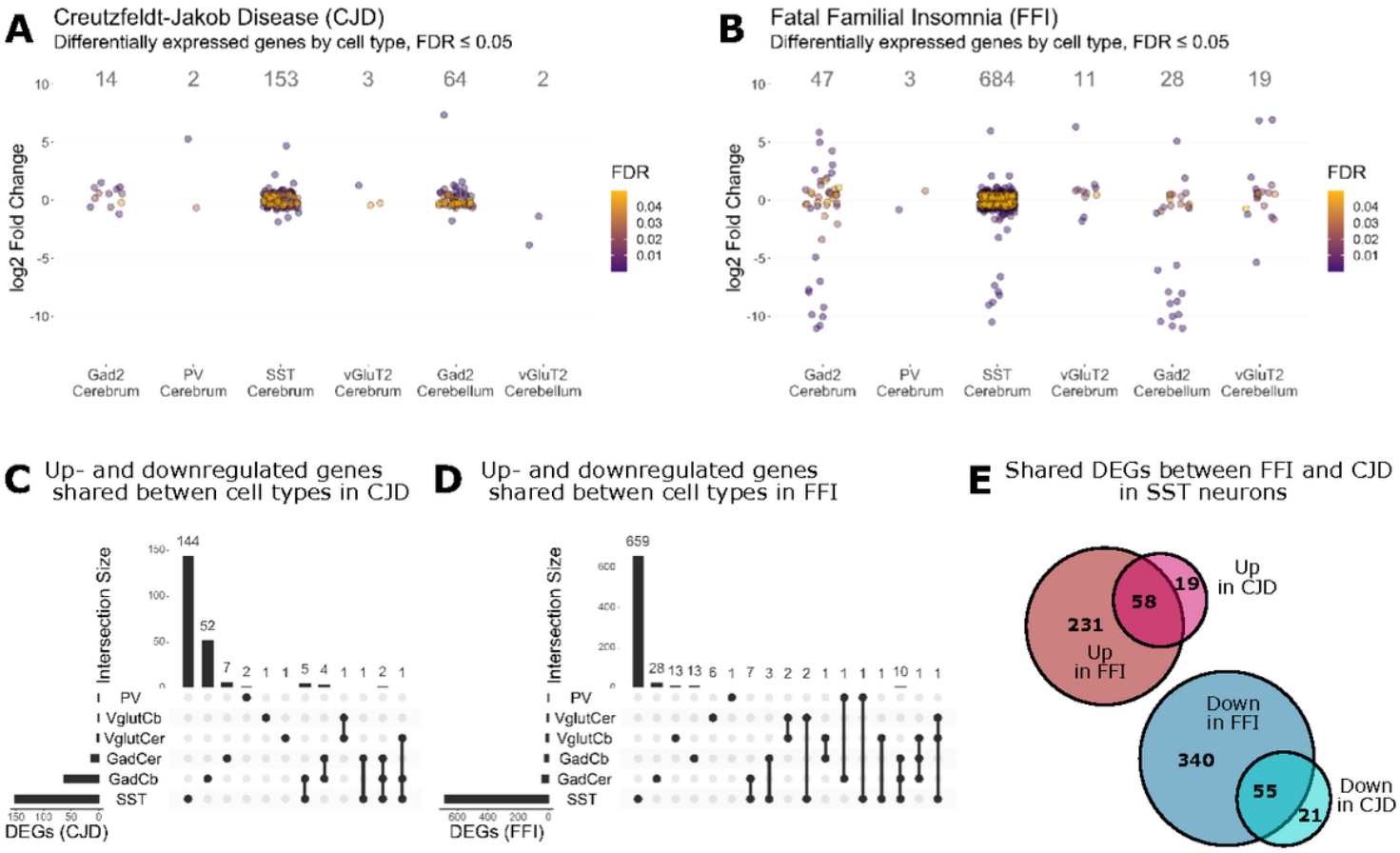

Figure 4

Differential gene expression analysis suggest strong expressional changes in SST+ neurons in CJD and FFI.

(A, B) Zoom in of dotplots showing significantly (FDR ≤ 0.05) differentially expressed genes (DEGs) by cell type in CJD (A) and FFI (B), respectively compared with control cells. See Fig. S3 for full sized plots. **(C, D)** Number of DEGs shared between cell (method = "Resnik", threshold = 0.8). **(E)** Number of up- and downregulated DEGs by disease models in SST^{+} neurons.

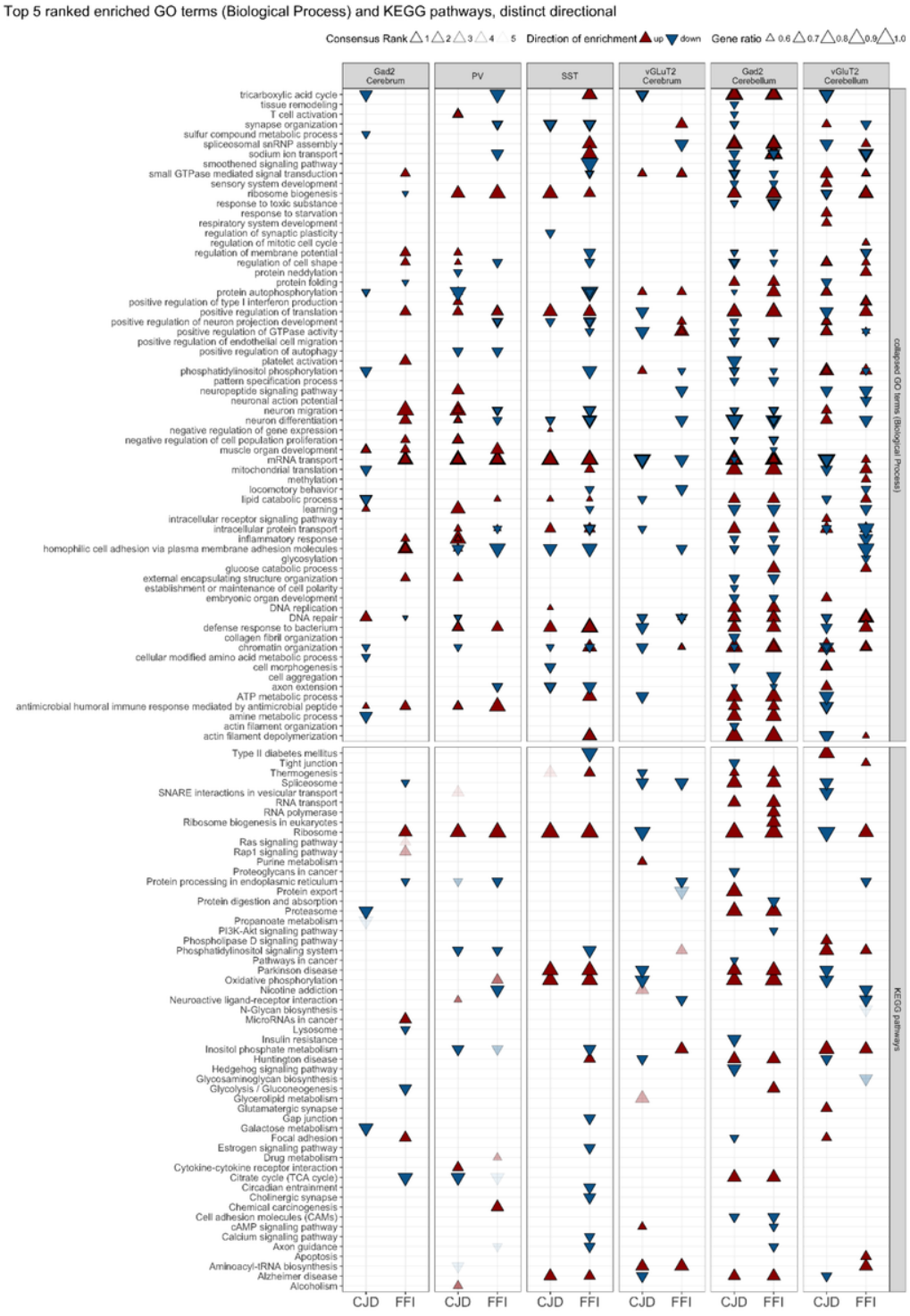

Figure 5

Gene set analysis suggests targeted GABAergic cell types show similar responses in CJD and FFI

Minimal consensus scores were calculated based on multiple gene set statistics for distinct up- and downregulated gene sets. GO Biological Process terms and KEGG pathways with FDR-adjusted p-value ≤ 0.05 in at least three of the six applied gene set statistical analyses and a consensus rank of ≤ 5 are displayed. The gene ratio indicates the number of genes changed in the indicated direction relative to total

genes in the set. For visualization, GO terms were collapsed based on semantic similarity (method = “Resnik”, threshold = 0.8) to reduce redundancy. This resulted in GO results in some cases displaying metrics for several gene sets summarized under the listed parent term.

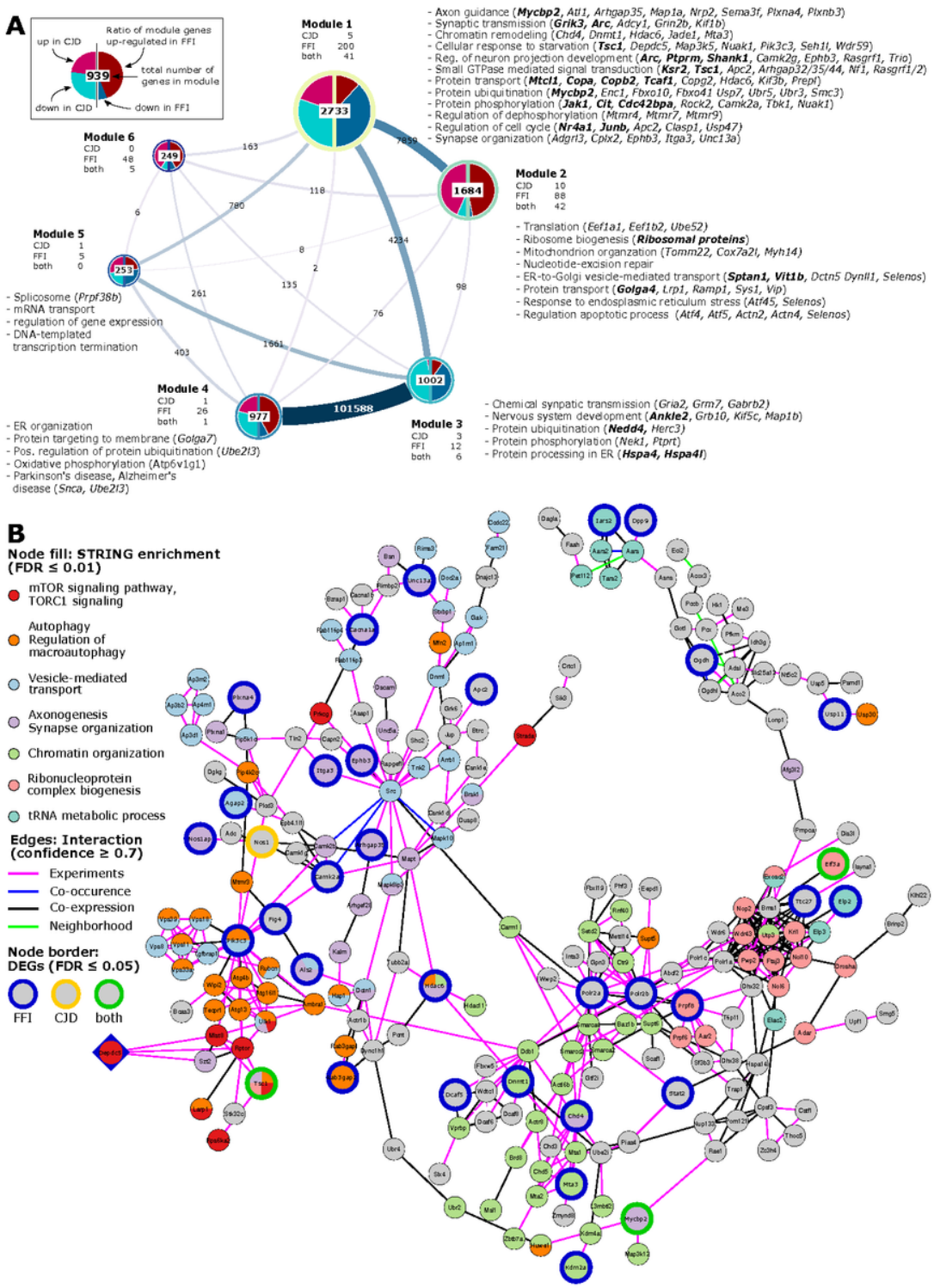

Figure 6

Network analysis SST+ neurons indicate mTOR signaling as central regulator of expressional changes.

(A) Visualization of identified modules for a SST^+ neuron weighted gene co-expression network with edges indicating inter-module connections. Half-pie charts displayed over the network nodes indicate the ratio of up- and down-regulated genes in CJD (left half) and FFI (right half). Labels indicate the number of module genes differentially expressed in CJD, FFI or both diseases. Significantly enriched GO terms (FDR ≤ 0.01) were collapsed by semantic similarity with selected parent terms, or enriched KEGG pathways (FDR ≤ 0.01) displayed in module annotations. Gene symbols in parentheses show a selection of annotated genes significantly differentially expressed in FFI (italics) or both diseases (bold italics). **(B)** Largest connected component of a protein-protein interaction network for module 1 hub gene *Depdc5* (diamond-shaped) and first-degree neighbors. Larger nodes with colored border indicate DEGs by disease. Node colors show selected functional associations of genes based on STRING enrichment (FDR ≤ 0.01).

Supplementary Files

This is a list of supplementary files associated with this preprint. Click to download.

- AdditionalFile1.pdf
- AdditionalFile2.xls
- AdditionalFile3.pdf
- AdditionalFile4.xls
- AdditionalFile5.pdf
- AdditionalFile6.pdf
- AdditionalFile7.xls
- AdditionalFile8.pdf
- AdditionalFile9.xls
- AdditionalFile10.xls
- AdditionalFile11.xls
- AdditionalFile12.pdf
- AdditionalFile13.pdf
- AdditionalFile14.pdf